Electronic Supplementary Material: Theoretical Study of the Structural and Energetic Properties of $Ce_{1-x}Zr_xO_2$ Nanoparticles via Molecular Dynamics Simulations

Mylena N. Santos,* Tuanan C. Lourenço,* Mauricio Mocelim,* and Juarez L. F. Da Silva*

São Carlos Institute of Chemistry, University of São Paulo, P.O. Box 780, 13560-970, *São Carlos, São Paulo, Brazil*

E-mail: mylenansantos@outlook.com; lourenco.tuanan@gmail.com; mauriciomocelim@hotmail.com; juarez_dasilva@iqsc.usp.br

Contents

S1 Introduction

This supplementary information contains additional computational details and results obtained in the investigation of the effects of particle size (number of atoms) and composition on the morphology, crystallization process, cation, and anion distribution in the $Ce_{1-x}Zr_xO_2$ nanoparticles.

S2 Additional Details on the Theoretical Methodology

S2.1 Molecular Dynamics Simulations

S2.1.1 Verlet Integration Algorithm

In order to obtain the positions of the ions at the time of integration (where the trajectory of nanoparticles over time is obtained by solving the equations of motion), the Verlet algorithm[1] is used, which is described by the Equation 1:

$$\mathbf{d}(t+\Delta t) = 2\mathbf{d}(t) - \mathbf{d}(t-\Delta t) + \mathbf{a}(t)\Delta t^2 \,, \tag{1}$$

so that, at time t, $\mathbf{d}(t)$ are the positions and $\mathbf{a}(t)$ the accelerations, whereas $\mathbf{d}(t+\Delta t)$ and $\mathbf{d}(t-\Delta t)$ are the positions in the next and previous moments, respectively. Δt is the integration time.

As shown in Equation 1, we note the absence of terms in relation to particle velocities, which is due to the fact that such an equation is the result of a Taylor series in relation to $\mathbf{d}(t)$:

$$\mathbf{d}(t+\Delta t) = \mathbf{d}(t) + \Delta t\mathbf{v}(t) + \frac{1}{2}\Delta t^2\mathbf{a}(t) + \dots \,, \tag{2}$$

$$\mathbf{d}(t-\Delta t) = \mathbf{d}(t) - \Delta t\mathbf{v}(t) + \frac{1}{2}\Delta t^2\mathbf{a}(t) - \dots \,, \tag{3}$$

summing Equations 2 and 3, eliminates the particle velocity terms, resulting in Equation 1. In this way, the calculation of speeds can be performed when necessary, using the following equation:

$$\mathbf{v}(t) = \frac{\mathbf{d}(t+\Delta t) - \mathbf{d}(t-\Delta t)}{2\Delta t} \,. \tag{4}$$

Other algorithms were developed based on this formulation in order to increase the accuracy of trajectory calculations, such as the "velocity-Verlet" algorithm, which is the standard method for solving motion equations in LAMMPS. Unlike Equation 1, this algorithm requires calculating velocities at intermediate time intervals ($\frac{1}{2}\Delta t$). In this way, velocities ($\mathbf{v}$) and positions $\mathbf{d}$ are

calculated by the following equations[2]:

$$\mathbf{d}(t+\Delta t) = \mathbf{d}(t) + \frac{1}{2}\Delta t^2 \mathbf{a}(t) + \Delta t \mathbf{v}(t) \ , \tag{5}$$

$$\mathbf{v}(t+\Delta t) = \mathbf{v}(t) + \frac{1}{2}\Delta t [\mathbf{a}(t) + \mathbf{a}(t+\Delta t)] \ . \tag{6}$$

The new positions and velocities in time $t+\Delta t$ are obtained in a process of 4 steps: (*i*) the new positions **R** are obtained using Equation 5. Once the positions have been obtained, (*ii*) the velocities are obtained at intermediate times as follows:

$$\mathbf{v}(t+\frac{1}{2}\Delta t) = \mathbf{v}(t) + \frac{1}{2}\Delta t^2 \mathbf{a}(t) \ . \tag{7}$$

Then, (*iii*) the forces and accelerations in the time $t+\Delta t$ are then calculated, and (*iv*) the velocities in the following time $(t+\Delta t)$ are obtained by:

$$\mathbf{v}(t+\Delta t) = \mathbf{v}(t+\frac{1}{2}\Delta t) + \frac{1}{2}\Delta t \mathbf{a}(t+\Delta t) \ . \tag{8}$$

At the end of this process, the algorithm is restarted and executed again at each integration time until the end of trajectory propagation, that is, until the end of the simulation.

S2.1.2 Temperature and Pressure Control

To compare the simulation and experimental results, it is necessary to work with constant temperature and pressure,[3,4] and the control of these thermodynamic properties can be done through the use of thermostats and barostats algorithms. Temperature and pressure can be controlled by modifying Newtonian equations of motion or particle velocities during the simulation.[4] With regard to isothermal-isochoric simulations, canonical ensemble, NVT, one of the most widely used thermostats[4,5] is Nosé-Hoover's, implemented in the LAMMPS package. Providing the strictest temperature control[3], through velocity scaling. This method is based on extending the system, where the temperature is controlled by introducing a thermal bath and an additional degree of freedom: a term for the system mass.[3–5] Similar to the temperature control approach is pressure control,[3] which can be performed by scaling the system volume.[3]

The Nosé-Hoover barostat, associated with the isothermal-isothermal ensemble, NpT, is also implemented in LAMMPS.

S2.1.3 Initial Generation of the $Ce_{1-x}Zr_xO_2$ Nanoparticles

Considering the Ce_nO_{2n} stoichiometry, the syntheses of nanoparticles containing 96 (32 Ce ions) to 768 (256 Ce ions) atoms were simulated. The particle sizes were obtained from a Crystallographic Information File for cerium oxide. The unit cell, containing 12 atoms (4 Ce ions), was expanded in three dimensions, constituting the supercell with sizes $2 \times 2 \times 2$, $3 \times 3 \times 2$, $3 \times 3 \times 3$ and $4 \times 4 \times 4$.

In order to find a better final configuration for the intermediate NP, the simulations were performed again, and the best configuration is shown in Figure S1, which contains the eight system sizes. During the development of this research, eight different sizes for CeO_2 nanoparticles were studied: $Ce_{40}O_{80}$, $Ce_{56}O_{112}$, $Ce_{140}O_{280}$ and $Ce_{198}O_{396}$; respectively, 120, 168, 420 and 594 atoms. Analogous monoclinic and tetragonal zirconia nanoparticles were also obtained. Figure S2–S3 shows all reference nanoparticles.

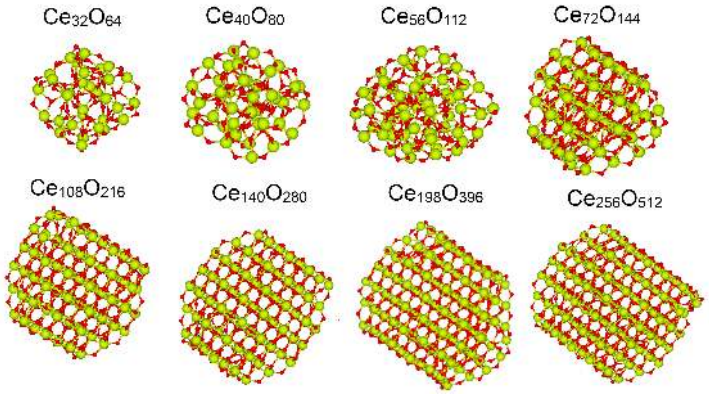

Figure S1: Molecular representation for initial CeO_2 NPs. Lime and red indicate the Ce^{4+} and O^{2-} ions, respectively.

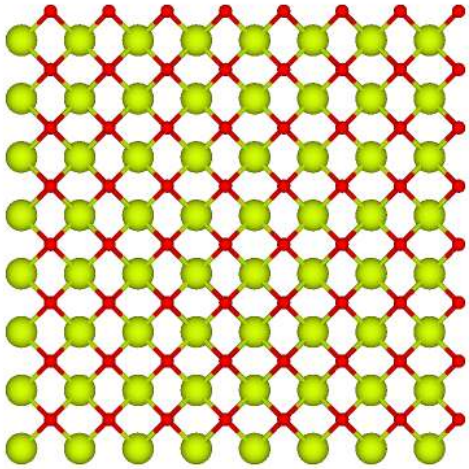

Figure S2: Ceria reference bulk system, fluorite-like cubic structure, containing 256 cations. Lime and red indicate the Ce^{4+} and O^{2-} ions, respectively.

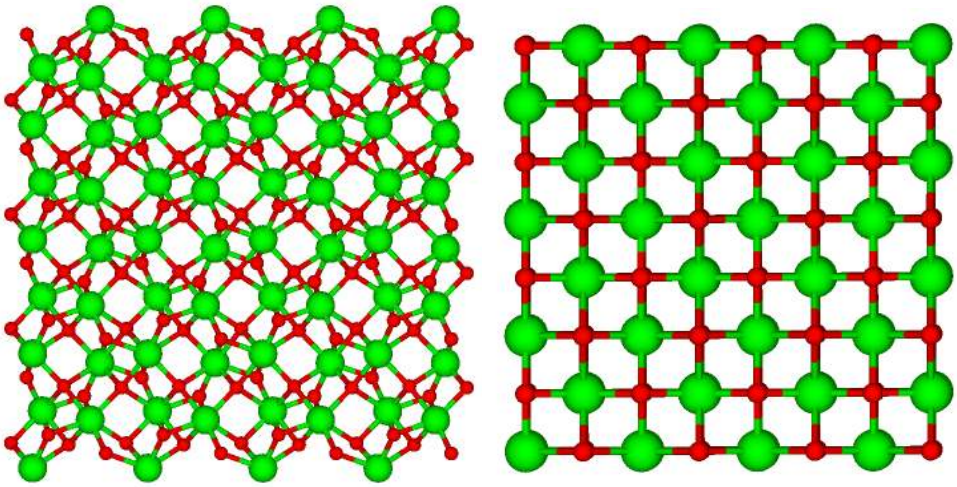

Figure S3: Monoclinic zirconia reference bulk system on the left and a tetragonal ZrO_2 bulk on the right, all containing 256 cations. Green and red indicate the Zr^{4+}, and O^{2-} ions, respectively.

S2.1.4 Amorphization-recrystallization Protocol

The recrystallization step, or annealing, consisted of decreasing the temperature at equivalent temperature ramps of $100\,\mathrm{K\,ns^{-1}}$. The temperature was decreased during 1 ns and in the next step, was kept constant for another 1 ns, until the end of the simulation. In this way, the temperature was reduced every 100 K, completing at the end 112 ns, as applied in a recently published work of the group[6]. In addition, the protocol for this step was improved by fixing the linear and angular moments, as well as the particle in the center of the box, in order to avoid segregation of the structure.

The recrystallization protocol for nanoparticles with sizes larger than 108 cations is shown below.

- From 5500 K to 4500 K, the temperature decreased 50 K ns^{-1} in 1 ns simulation and was constant for another 1 ns, since the temperature was far from the melting point and considering the computational cost as well;
- After 4500 K, we used a Δ_{Temp} of 20 K ns^{-1} for 1 ns in the annealing steps until 2500 K, since the temperature range comprises the phase transition temperature;
- From 2500 K the temperature decreased in a Δ_{Temp} of 50 K ns^{-1} until 500 K;
- From 500 K until 0.001 K the temperatures decreased in steps of 100 K ns^{-1}. In the end, the simulation trajectories for these NPs have a total time of 330 ns.

S2.2 Density Functional Theory Calculations

For all density functional theory calculations, we applied the projector augmented wave (PAW) method, and the Table S1 shows the most important information regarding PAW projectors. In order to obtain more accurate results, we use the GW variant among those available for each element.

Table S1: Most important details regarding the PAW-PBE projectors used in this work: Chemical species, name of the projectors with date of creation, highest recommended cutoff energy for the plane-wave basis set, `ENMAX`, in eV, the number of valence electrons, Z_{val}, and the electronic configuration of the valence states.

Element	PAW-PBE projector	`POTCAR` date	`ENMAX`	Z_{val}	Valence
O	O_GW	09/28/2005	414.635	6	$2s^2 2p^4$
Ce	Ce_GW	03/26/2009	304.625	12	$5s^2 6s^2 5p^6 5d^1 4f^1$
Zr	Zr_sv_GW	12/05/2013	346.364	12	$4s^2 4p^6 4d^4$

S3 Computational Tests for the Amorphization-recrystallization Process via MD Simulations

In order to obtain even more organized structures in our molecular dynamics (MD) simulations, some tests for the amorphization and annealing protocol were carried out, keeping in mind that more organized structures would certainly be obtained through the separation of processes and a greater detailing of the simulations. The tests were also carried out taking into account the simulations that failed. Considering the computational cost of the simulations, these were first performed for intermediate NP. From the results, a more defined protocol was used for the larger NP. The comparison of the results was made from the observation of the final structures, detailed below.

S3.1 Differences Between the Initial and Final Simulations Protocol

The second amorphization step was previously integrated with the recrystallization, performed immediately before the latter. Furthermore, while in the first stage, the temperature was raised to 8500 K, in the second it was reduced to the temperature from which the recrystallization simulation would be performed. Previously, for the first stage, a Lennard–Jones wall referring to the 12/6 potential with different parameters was used: σ, ε, and the cutoff distances of 1.0 Å, 5.0 eV Å^{-2} and 5.0 Å.

With the new protocol, the first amorphization step is performed by reducing the temperature from 10 500 to 5500 K, and at the end of the simulation a command is used to guarantee obtaining a centralized and nucleated particle, which is important for the success of the second amorphization step. In the annealing, we removed the walls with the new protocol in order to allow greater movement of the particle in the box, considering the already used commands for the particle to be kept in the center and have its moments reset to zero with the given frequency. The walls were not used in the second amorphization stage this time, for the same reason, considering that the particle was re-centered at the end of the previous stage.

S3.2 Morphology Referring to the Initial Simulation Protocol

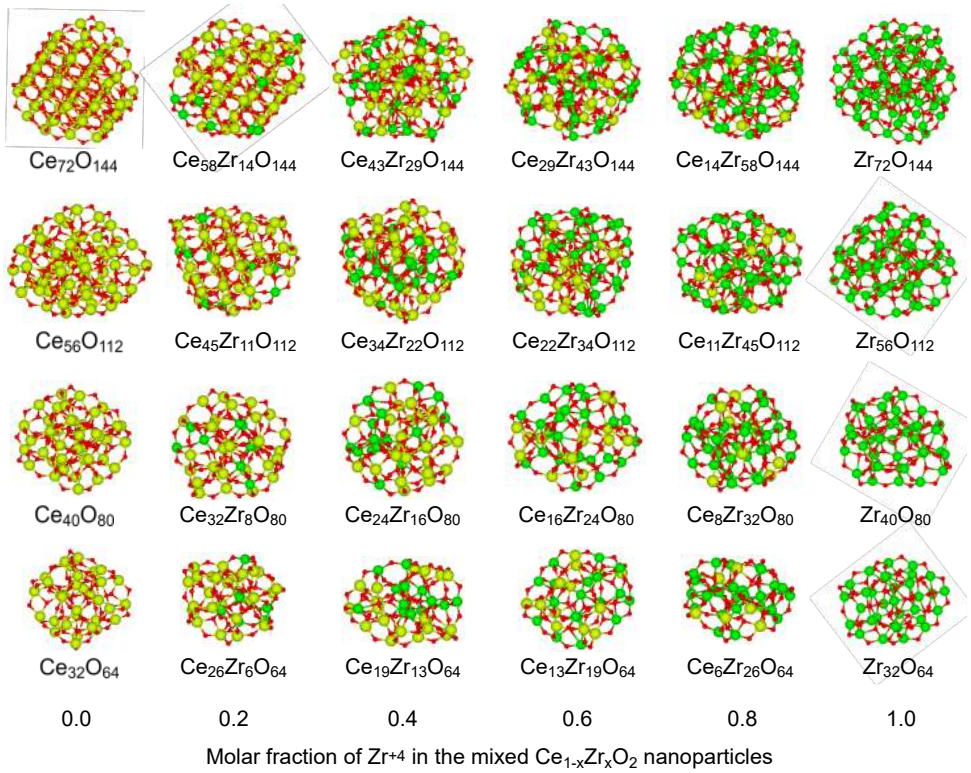

Figure S4: Molecular representation of all the sizes and compositions for the $Ce_{1-x}Zr_xO_2$ NPs with up to 72 cations at 0 K, generated from the initial protocol of simulations. Lime, green, and red indicate the Ce^{4+}, Zr^{4+}, and O^{2-} ions, respectively.

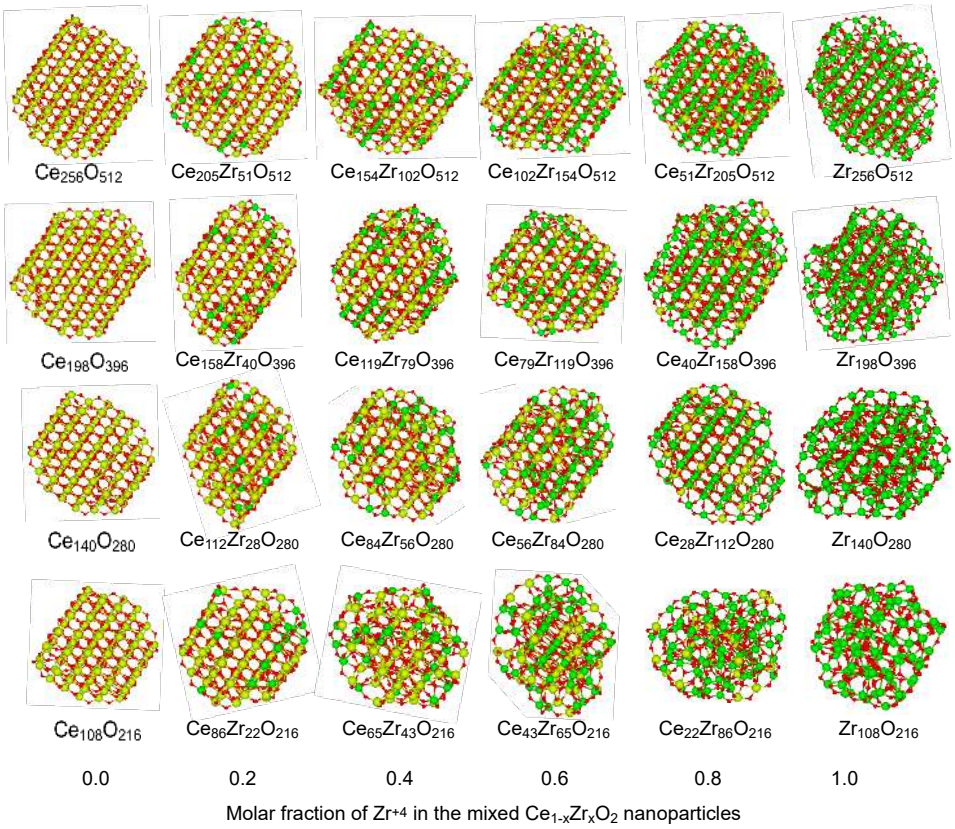

Figure S5: Molecular representation of all the sizes and compositions for the $Ce_{1-x}Zr_xO_2$ NPs with more than 72 cations at 0 K, generated from the initial protocol of simulations. Lime, green, and red indicate the Ce^{4+}, Zr^{4+}, and O^{2-} ions, respectively.

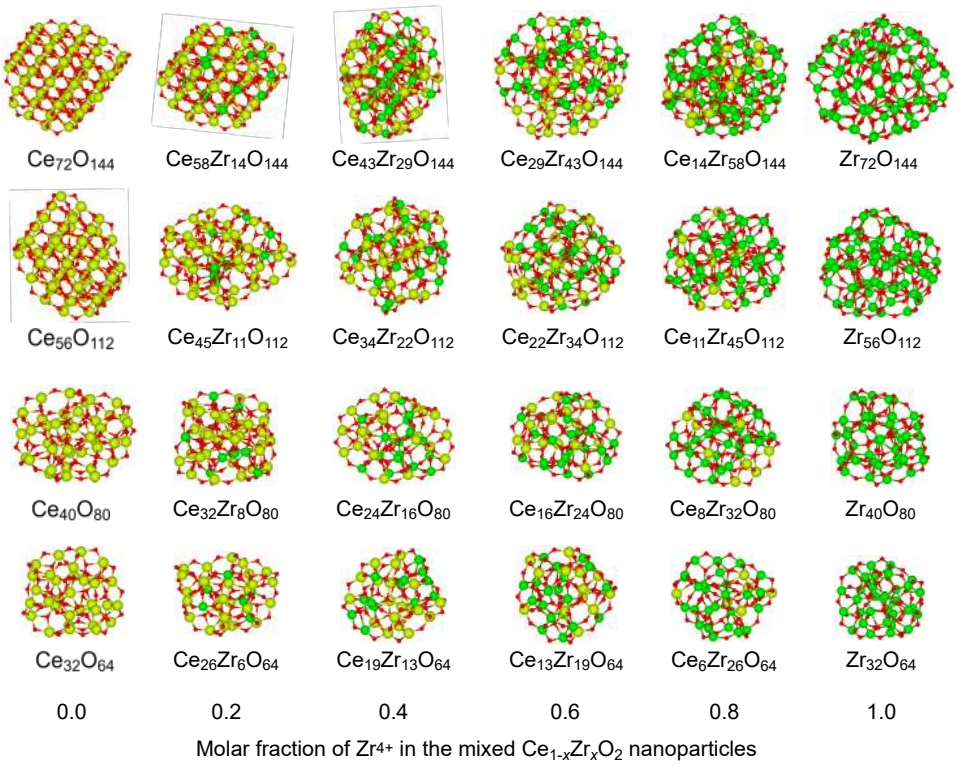

Figure S6: Molecular representation of all the sizes and compositions for the $Ce_{1-x}Zr_xO_2$ NPs with up to 72 cations at 0 K, generated from the final protocol of simulations. Lime, green, and red indicate the Ce^{4+}, Zr^{4+}, and O^{2-} ions, respectively.

Figure S4–S5 shows the final structures of the NP. From morphological analysis, we observed (111) planes on the surfaces of the structures of $Ce_{72}O_{144}$ and larger sizes. We did not observe the same for zirconia NP. For NPs with a maximum molar fraction of 0.20 of Zr^{+4}, there are more ordered structures, especially the NPs $Ce_{45}Zr_{11}O_{112}$ and $Ce_{58}Zr_{14}O_{144}$. A larger molar fraction of Zr^{+4} induces loss of organization and more spherical morphology. Thus, the increase in the concentration of zirconium leads to an increase in the distortion of the structure. For Zr NP, the (111) planes occur for $Zr_{108}O_{216}$ and larger sizes. The rounded shape of the nanoparticles is less evident as the size of the NPs increases.

S3.3 Morphology Referring to the Final Simulation Protocol

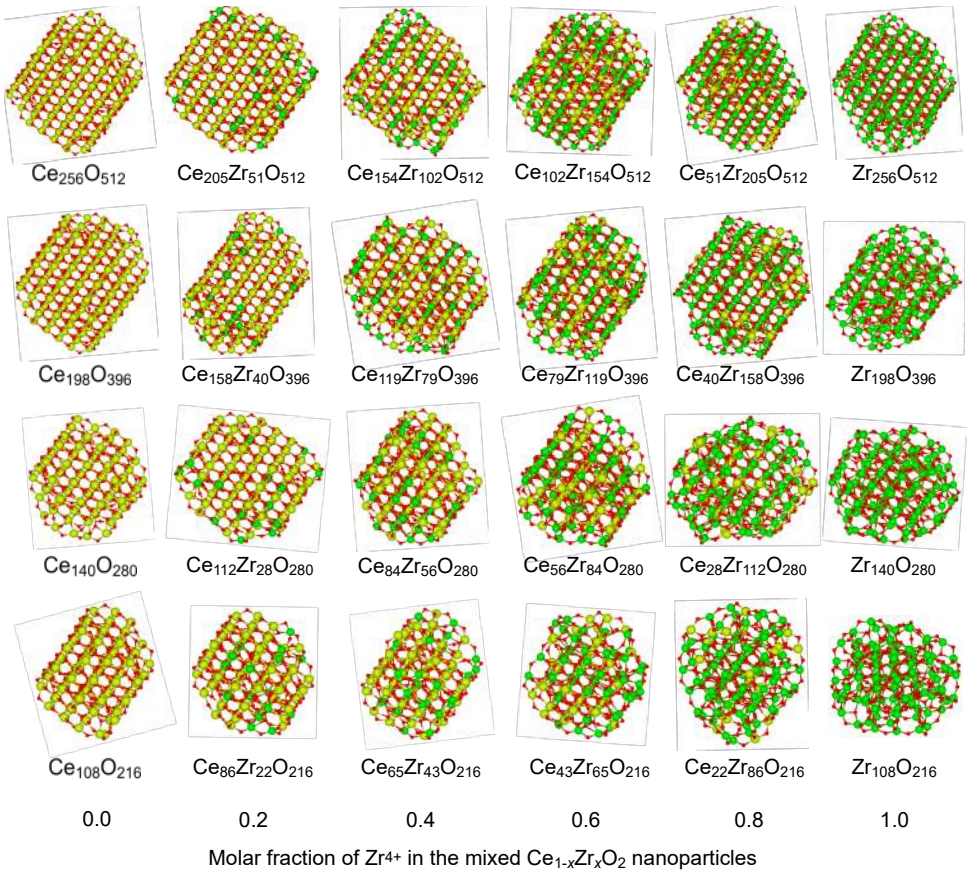

Figure S7: Molecular representation of all the sizes and compositions for the $Ce_{1-x}Zr_xO_2$ NPs with more than 72 cations at 0 K, generated from the final protocol of simulations. Lime, green, and red indicate the Ce^{4+}, Zr^{4+}, and O^{2-} ions, respectively.

Figure S7 shows that the fluorite type structure was observed for $Ce_{56}O_{112}$ and larger sizes, with the occurrence of planes of lower energy and format closer to the truncated octahedra. In the case of zirconia nanoparticles, the lower limit was maintained. However, in general, it is possible to notice that the structures were more ordered. All NPs containing more than 108 cations have a well-defined structure, and the difference in behavior with the variation in the molar fraction of zirconium is not significant. In the case of NPs containing less than 108 cations, the dependence on size and composition is more evident.

S3.4 Comparison Between the Morphologies from the Different Simulations Protocols

With the initial protocol of simulations, only $Ce_{72}O_{144}$ and $Zr_{108}O_{216}$ and larger sizes presented the truncated octahedra morphology. With the final protocol, we observed the truncated octahedra for $Ce_{56}O_{112}$ and larger sizes. For zirconia nanoparticles, the lower limit was maintained. However, in general, it is possible to notice that the structures, even relative to the smaller NP, were more ordered.

S4 Additional Results

In this section, we discuss results not entirely shown in the manuscript, namely, additional phase transition data, morphology, total radial distribution function, X-ray diffraction, and energetic properties, including MD, molecular mechanics (MM) and density functional theory (DFT) results.

S4.1 Phase Transition

S4.1.1 Potential Energy as a function of Temperature

In this section, the figures relating to the relative potential energy in function of the temperature, Figures S8–S11, are shown, organized by system size, in order to provide better visualization of these graphics.

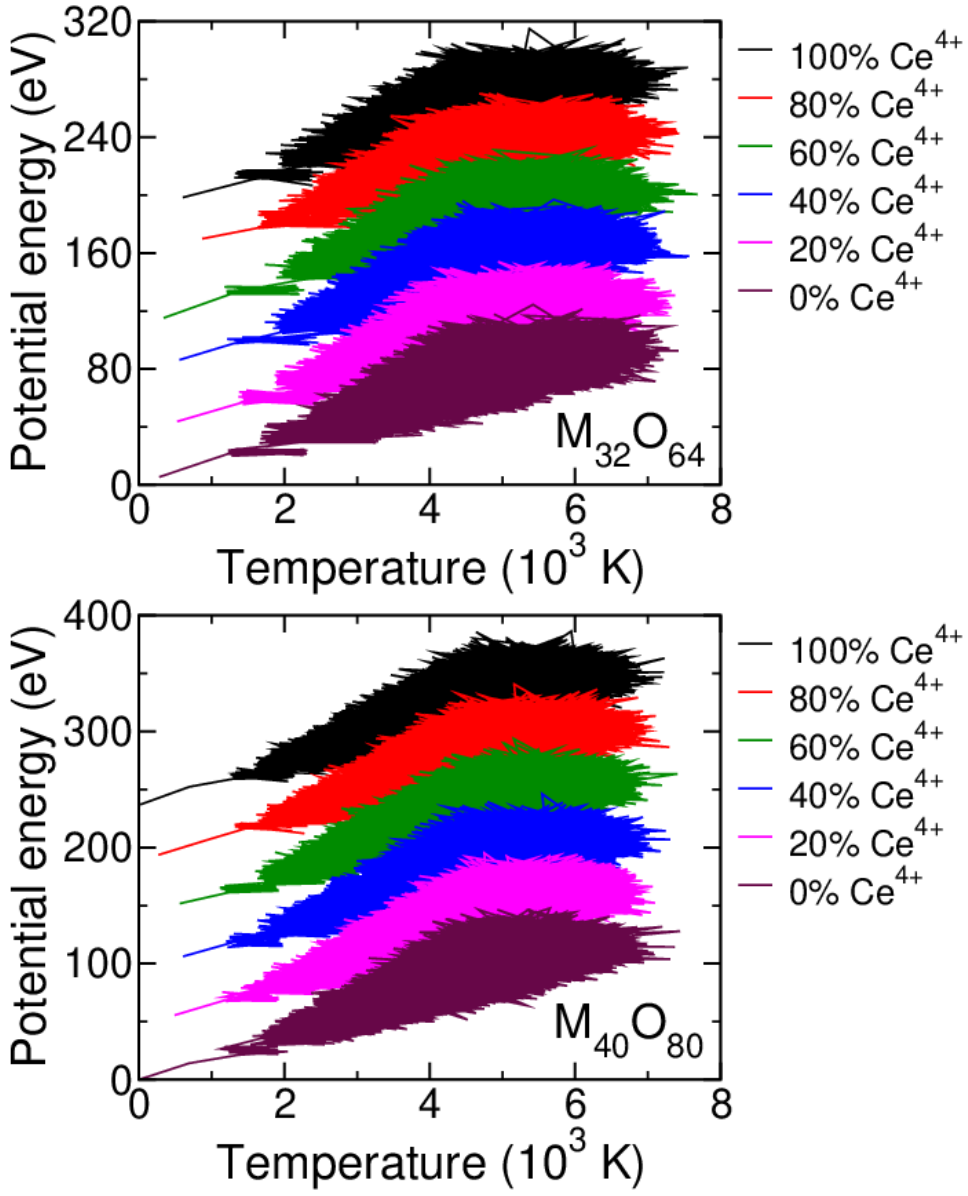

Figure S8: Relative potential energy, from MD simulations, in function of temperature. Results for the NPs with 32 and 40 cations.

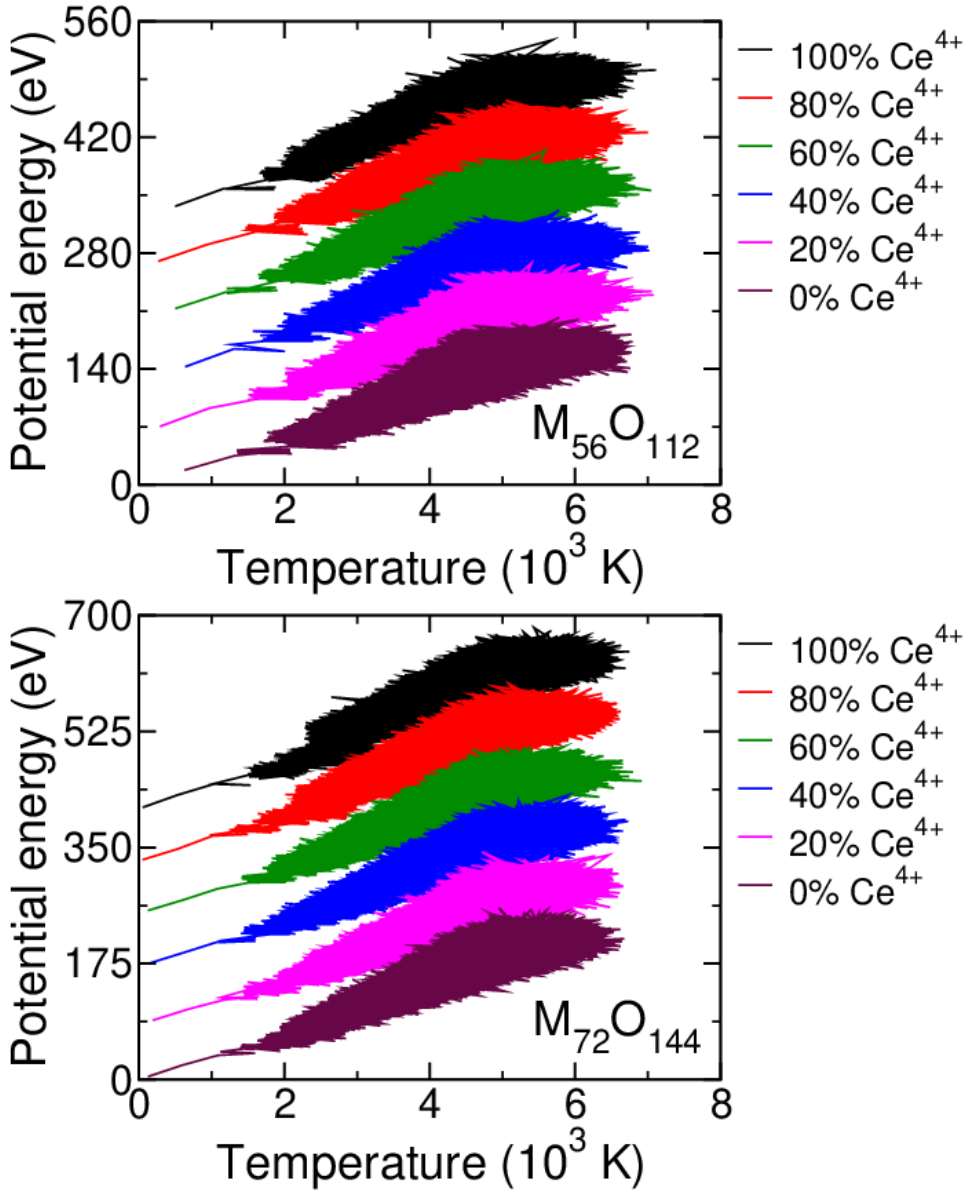

Figure S9: Relative potential energy, from MD simulations, in function of temperature. Results for the NPs with 56 and 72 cations.

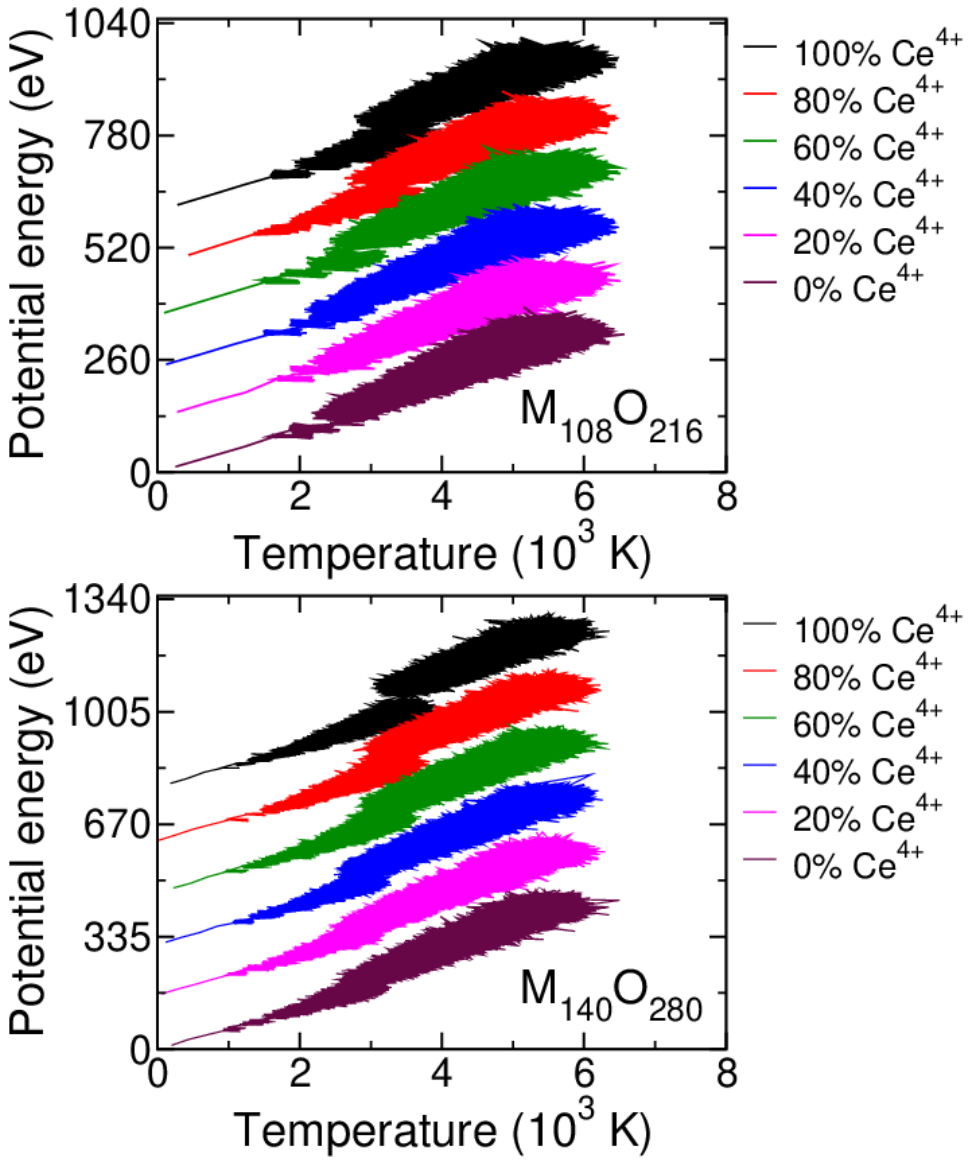

Figure S10: Relative potential energy, from MD simulations, in function of temperature. Results for the NPs with 108 and 140 cations.

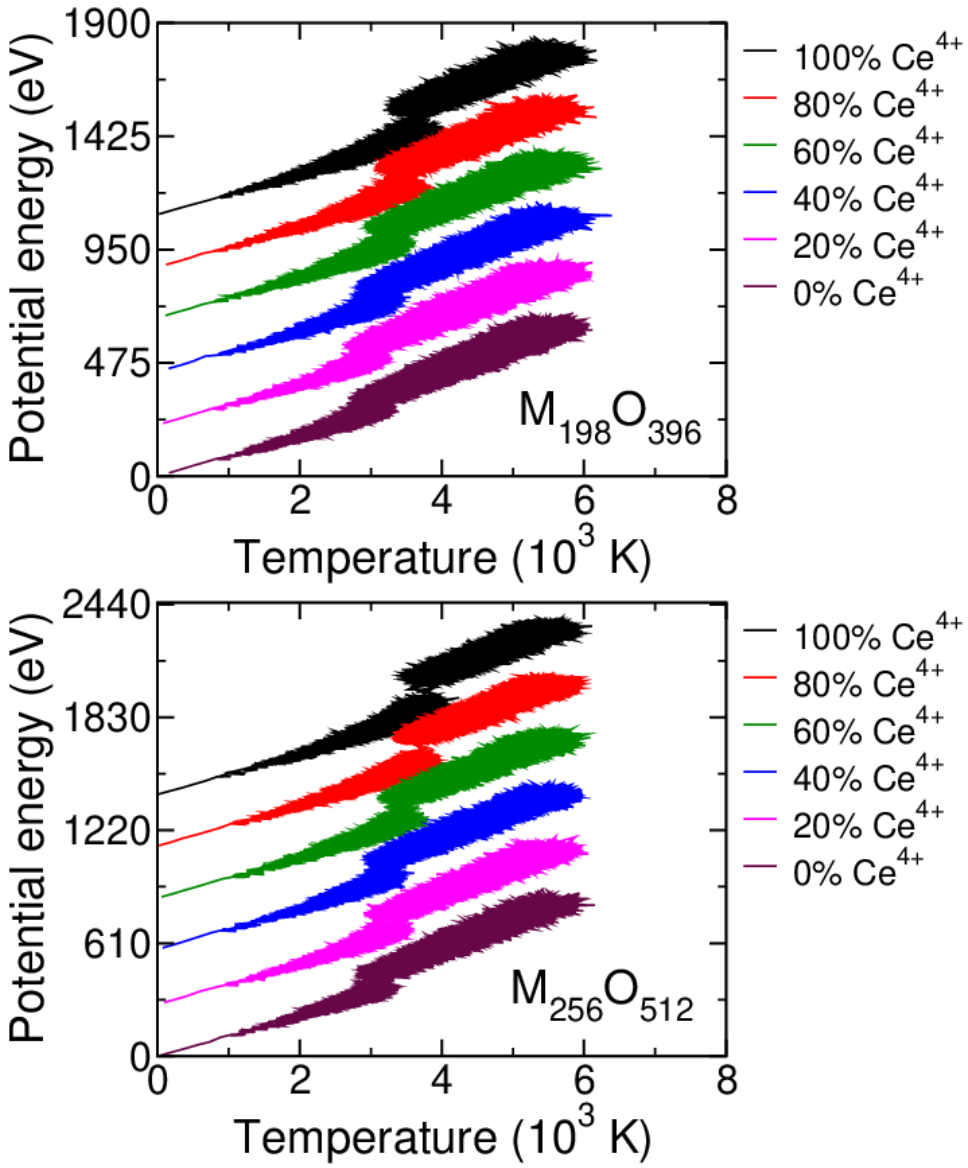

Figure S11: Relative potential energy, from MD simulations, in function of temperature. Results for the NPs with 198 and 256 cations.

S4.1.2 Phase Transition Temperatures

Table S2 shows the estimated phase transition temperature values, based on the analysis of the graphs in the previous section, the curves resulting from the point averages, and observing the change in the morphology of the structures with the reduction in temperature.

Table S2: Phase transition temperatures, T_{pt}, obtained for all the $Ce_{1-x}Zr_xO_2$ NPs. In parentheses, the number of cations with ordered crystal domain.

Size	x	System	T_{pt} (K)	Size	x	System	T_{pt} (K)
32 cations	0.0	$Ce_{32}O_{64}$	–	108 cations	0.0	$Ce_{108}O_{216}$	3385 (31)
	0.2	$Ce_{26}Zr_6O_{64}$	–		0.2	$Ce_{86}Zr_{22}O_{216}$	3160 (28)
	0.4	$Ce_{19}Zr_{13}O_{64}$	–		0.4	$Ce_{65}Zr_{43}O_{216}$	2810 (22)
	0.6	$Ce_{13}Zr_{19}O_{64}$	–		0.6	$Ce_{43}Zr_{65}O_{216}$	2515 (13)
	0.8	$Ce_6Zr_{26}O_{64}$	–		0.8	$Ce_{22}Zr_{86}O_{216}$	2180 (6)
	1.0	$Zr_{32}O_{64}$	–		1.0	$Zr_{108}O_{216}$	2520 (3)
40 cations	0.0	$Ce_{40}O_{80}$	–	140 cations	0.0	$Ce_{140}O_{280}$	3450 (45)
	0.2	$Ce_{32}Zr_8O_{40}$	–		0.2	$Ce_{112}Zr_{28}O_{280}$	3345 (43)
	0.4	$Ce_{24}Zr_{16}O_{40}$	–		0.4	$Ce_{84}Zr_{56}O_{280}$	3235 (44)
	0.6	$Ce_{16}Zr_{24}O_{40}$	–		0.6	$Ce_{56}Zr_{84}O_{280}$	2880 (30)
	0.8	$Ce_8Zr_{32}O_{40}$	–		0.8	$Ce_{28}Zr_{112}O_{280}$	2800 (38)
	1.0	$Zr_{40}O_{80}$	–		1.0	$Zr_{140}O_{280}$	2920 (15)
56 cations	0.0	$Ce_{56}O_{112}$	2485 (9)	198 cations	0.0	$Ce_{198}O_{396}$	3590 (73)
	0.2	$Ce_{45}Zr_{11}O_{112}$	–		0.2	$Ce_{158}Zr_{40}O_{396}$	3425 (65)
	0.4	$Ce_{34}Zr_{22}O_{112}$	–		0.4	$Ce_{119}Zr_{79}O_{396}$	3260 (59)
	0.6	$Ce_{22}Zr_{34}O_{112}$	–		0.6	$Ce_{79}Zr_{119}O_{396}$	3105 (56)
	0.8	$Ce_{11}Zr_{45}O_{112}$	–		0.8	$Ce_{40}Zr_{158}O_{396}$	2945 (57)
	1.0	$Zr_{56}O_{112}$	–		1.0	$Zr_{198}O_{396}$	3015 (40)
72 cations	0.0	$Ce_{72}O_{144}$	2770 (15[a])	256 cations	0.0	$Ce_{256}O_{512}$	3785 (104)
	0.2	$Ce_{58}Zr_{14}O_{144}$	2485 (12)		0.2	$Ce_{205}Zr_{51}O_{512}$	3625 (99)
	0.4	$Ce_{43}Zr_{29}O_{144}$	–		0.4	$Ce_{154}Zr_{102}O_{512}$	3455 (86)
	0.6	$Ce_{29}Zr_{43}O_{144}$	–		0.6	$Ce_{102}Zr_{154}O_{205}$	3200 (71)
	0.8	$Ce_{14}Zr_{58}O_{144}$	–		0.8	$Ce_{51}Zr_{205}O_{512}$	3260 (91)
	1.0	$Zr_{72}O_{144}$	–		1.0	$Zr_{256}O_{512}$	3080 (79)

[a] 13 fcc and 2 bcc cations. All the other NPs presented only fcc crystal domains.

S4.1.3 Phase Transition Temperatures, NP Size Effects

S4.1.4 Morphology of 108-Cations Structures with Temperature

In this section, we present the results of a morphological analysis complementary to those of the other sections regarding the phase transition. In this case, we show the 108-cation structures at 3 different temperatures: at 0 K, at the phase transition, and 1000 K above. We confirm the occurrence of phase transition following the change in morphology with the change in temperature, which is more evident as we reduce the dopant mole fraction. The phase transition

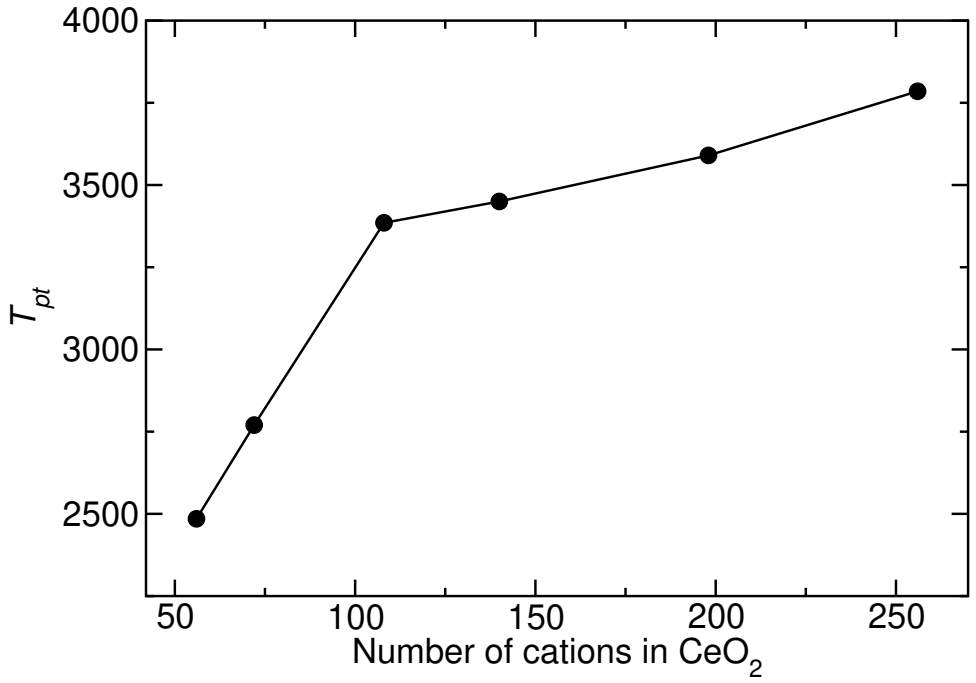

Figure S12: Effect of the NP size in the phase transition temperature for CeO_2.

temperature (T_{pt}) presented here is slightly different from those indicated in Table S2 because initially these temperatures had been estimated only based on the direct analysis of the graphs of potential energy vs. temperature.

Regarding the morphology at 0 K, the structures become less ordered as the molar fraction of zirconium increases. Following the graph and discussion related to Figure S13, the definition of the phase transition point is reduced as the relative amount of the dopant increases. The difference in the ordering of the NPs with a decrease in temperature is remarkable: the configurations related to the T_{pt} temperatures are more ordered than the temperatures 1000 K higher, but less ordered than at the end of the simulation. This is because the intermediate temperature is the temperature, which indicates the moment when the structure has crystal domains and has a faster tendency towards the final structure organization.

Figure S10 shows that it is not possible to observe clearly T_{pt} for a mole fraction of Zr^{4+} greater than 0.2. We can also observe this behavior in Figure S13 since there is not a significant difference regarding the crystalline domains and the occurrence of lower energy planes as the composition of the structure approaches pure zirconia. Even so, it is possible to observe that the above 1000 K structure is less ordered and presents a more irregular surface. At intermediate temperatures, the structures already have a format closer to the truncated octahedra.

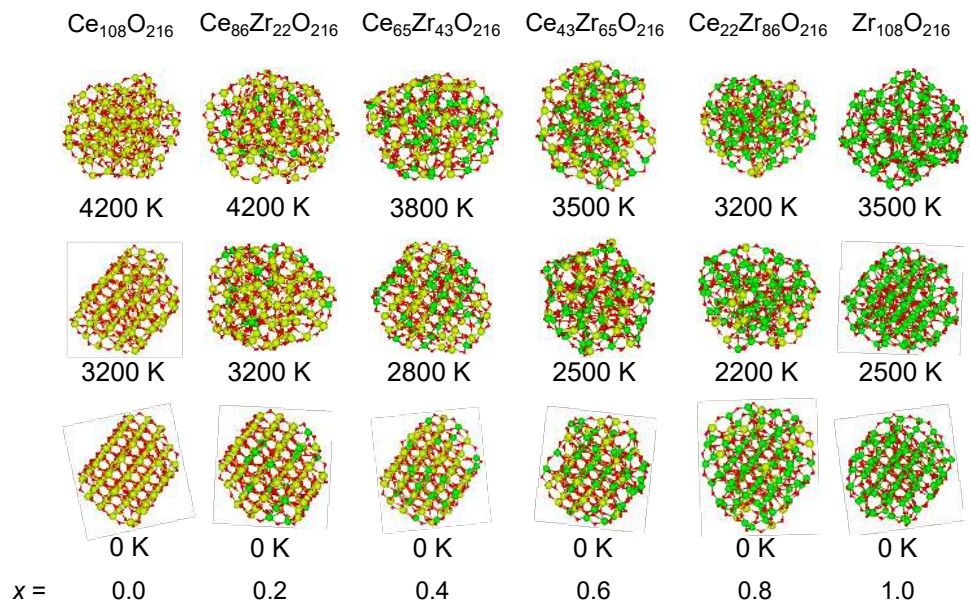

Figure S13: Molecular representation of all compositions of the NPs containing 108 cations at three different temperatures: Results for 0 K, T_{pt} (middle row) and $T_{pt} + 1000$ K (top row). Lime, green, and red indicate the Ce^{4+}, Zr^{4+}, and O^{2-} ions, respectively.

S4.2 Total Radial Distribution Functions

Figures S14 and S15 show a similar behavior independent of composition and temperature for NPs with up to 56 cations. This is evidence that these NPs do not have crystal domains. The crystalline domains are observed for the $Ce_{72}O_{144}$ and $Ce_{58}Zr_{14}O_{144}$ NP. As expected, the definition in the curves below the highest temperature and the difference between the curves for different temperatures decrease with increasing relative dopant concentration. In the case of NPs with 108 and 140 cations, Figure S16, this behavior is evidenced for NPs containing 198 and 256 cations, Figure S17.

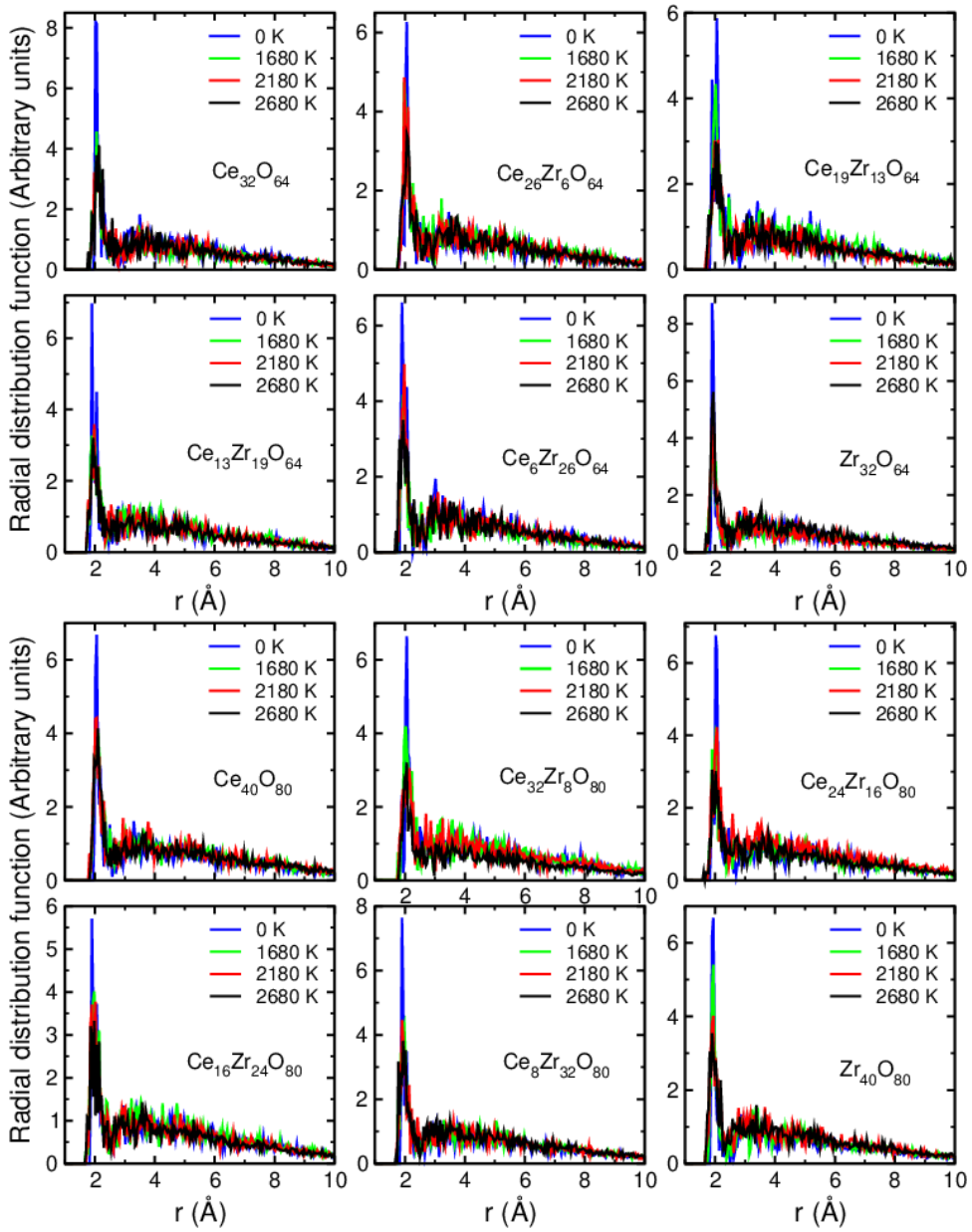

Figure S14: Total radial distribution functions for the NPs with 32 and 40 cations, at the temperatures of 0 K, T_{pt}, 500 K above and below T_{pt}.

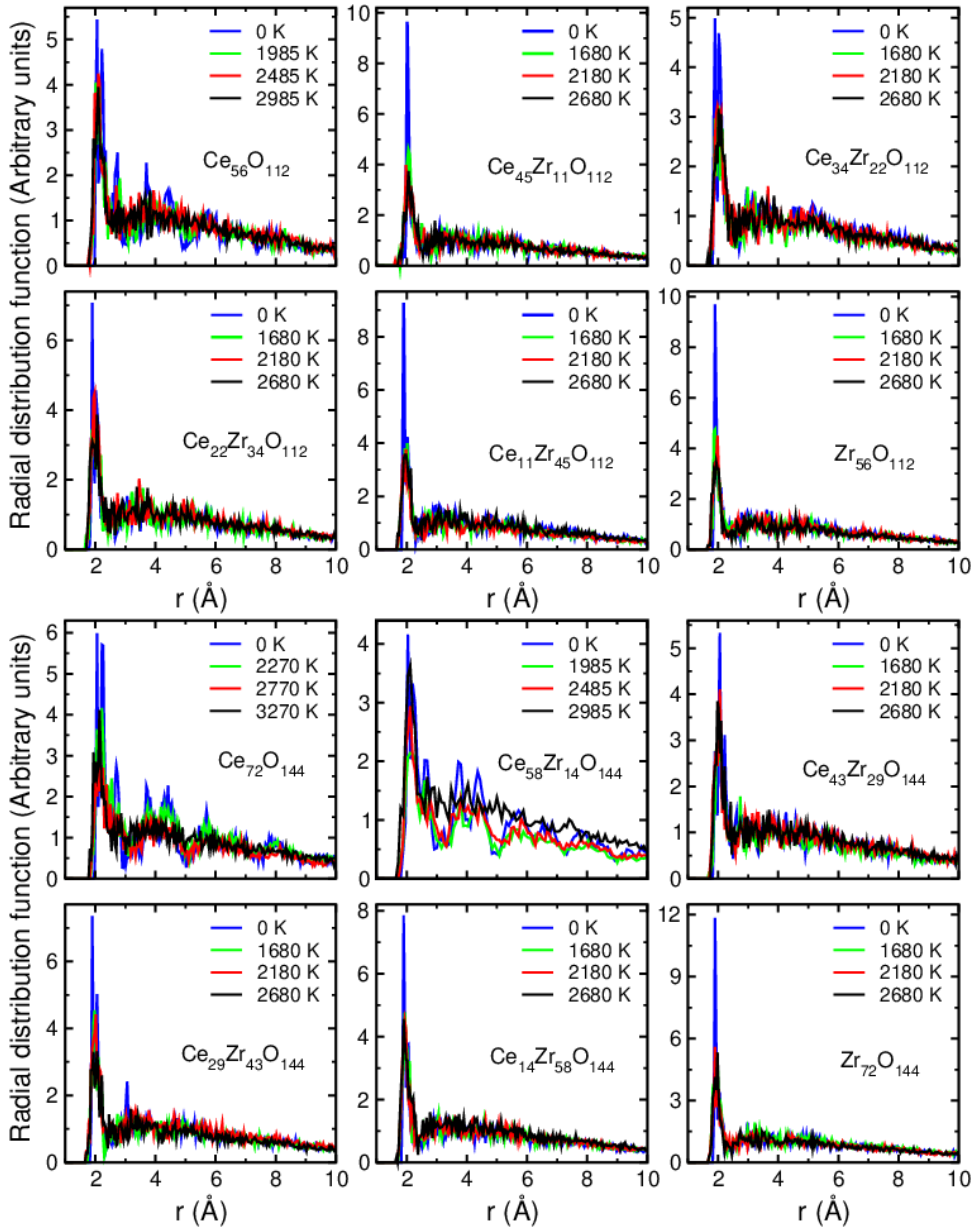

Figure S15: Total radial distribution functions for the NPs with 56 and 72 cations, at the temperatures of 0 K, T_{pt}, 500 K above and below T_{pt}..

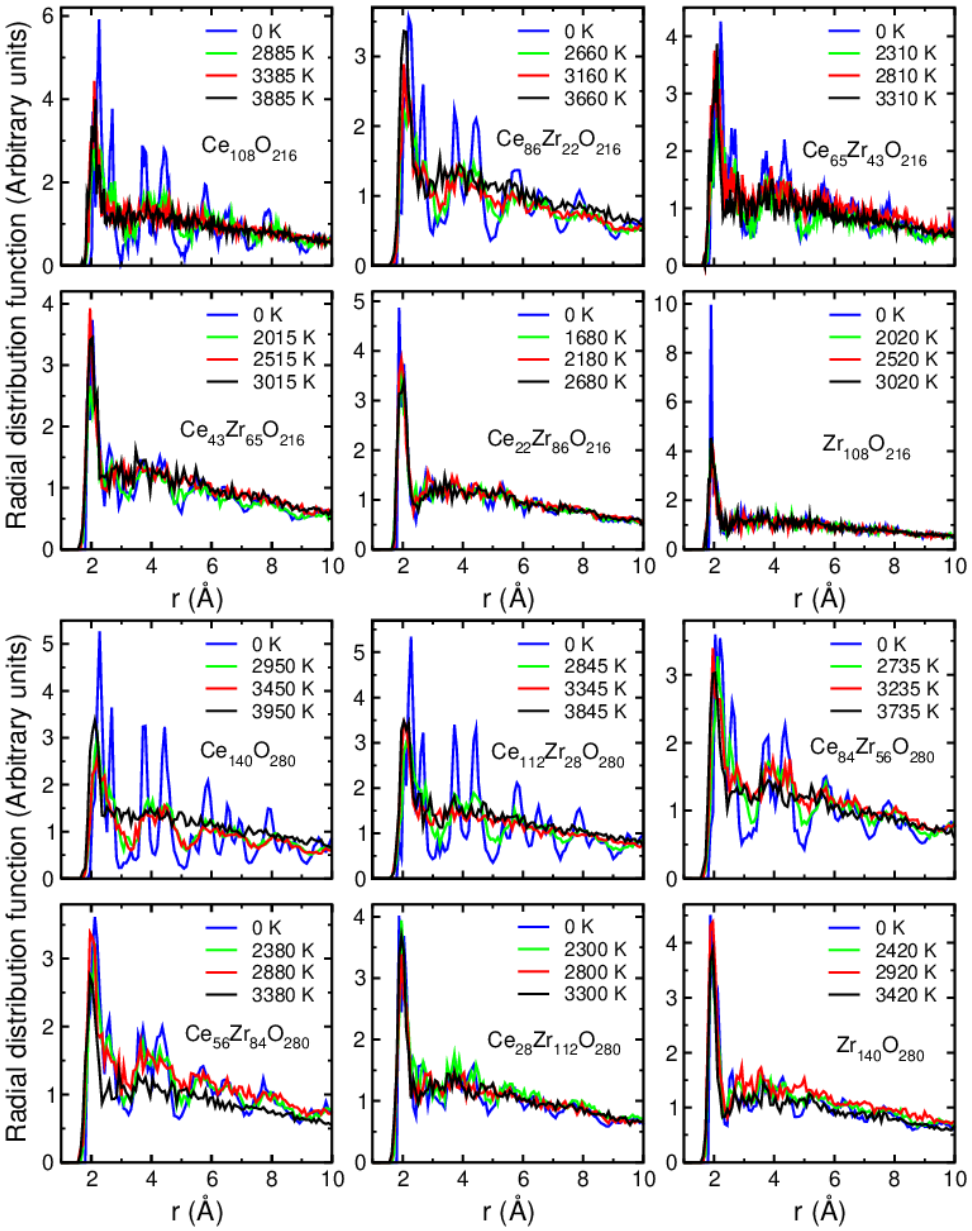

Figure S16: Total radial distribution functions for the NPs with 108 and 140 cations, at the temperatures of 0 K, T_{pt}, 500 K above and below T_{pt}..

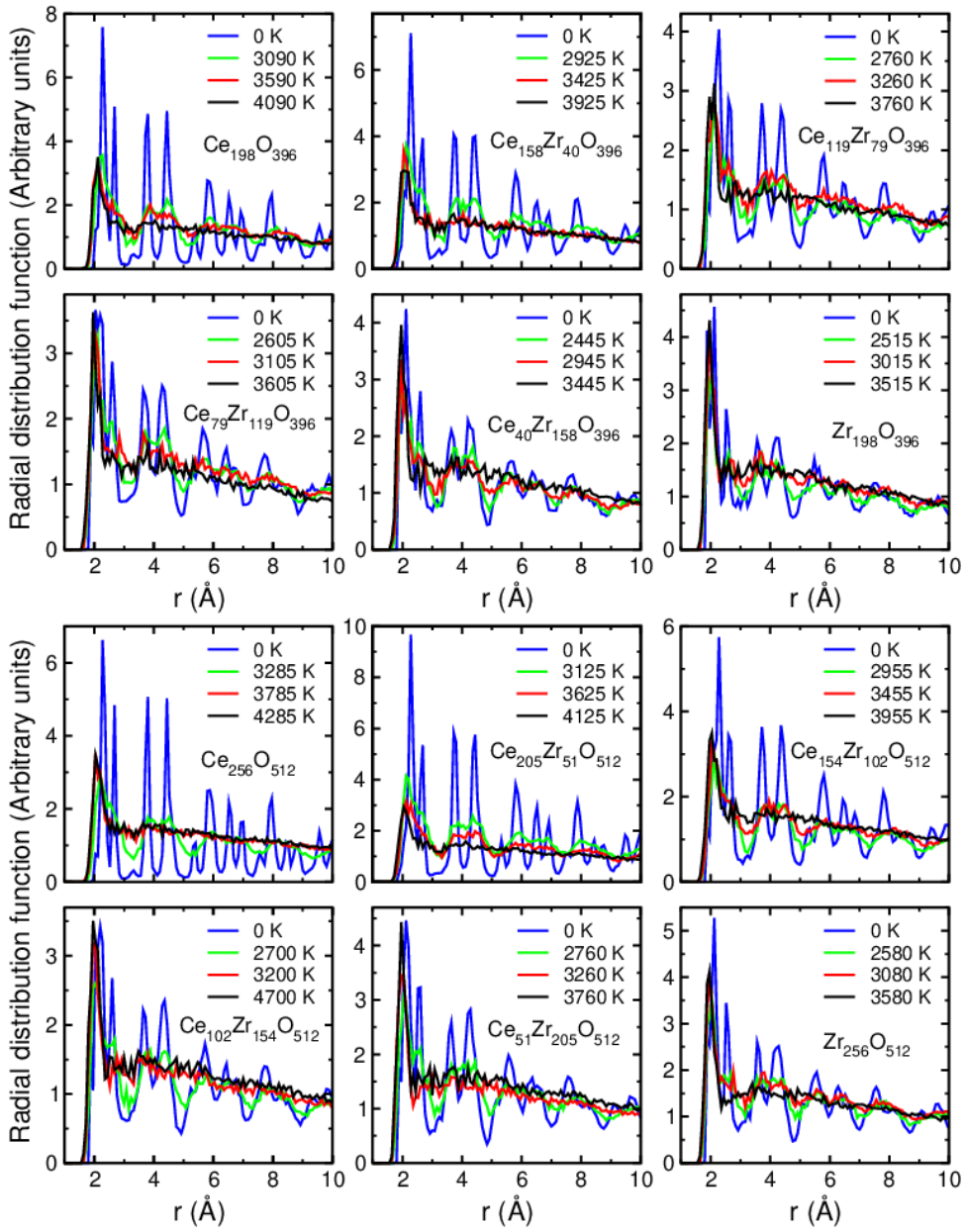

Figure S17: Total radial distribution functions for the NPs with 198 and 256 cations, at the temperatures of 0 K, T_{pt}, 500 K above and below T_{pt}..

S4.3 X-Ray Diffraction

The structure factor ($S(q)$) is a parameter involved in the X-ray diffraction analysis that is related to the atomic positions, but it is inversely proportional to the intensity of the scattered radiation ($I(q)$) and to the form factor ($P(q)$), which is associated with the shape and size of the particle: $S(q) = I(q)/P(q)$.[7,8]

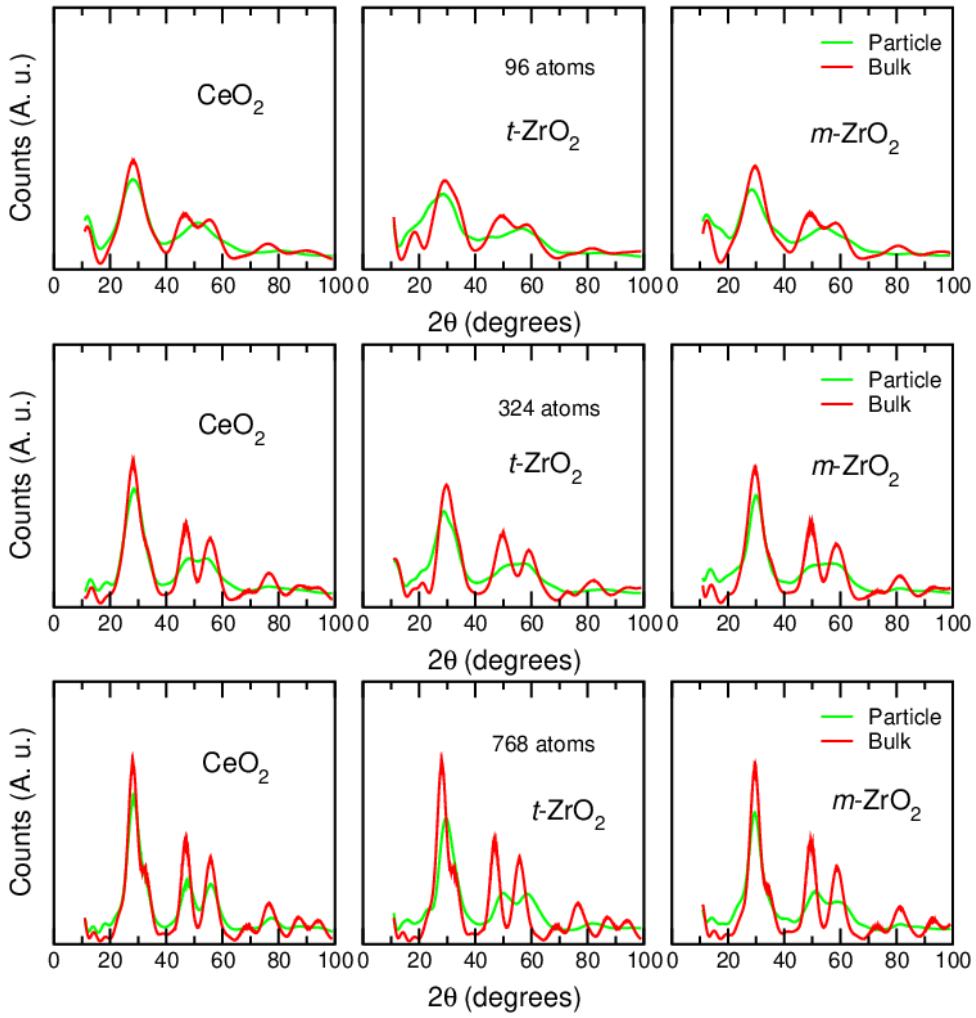

Figure S18: X-ray diffraction results for bulk and NPs of CeO_2, *t*-ZrO_2 and *m*-ZrO_2 with 32, 72 and 256 cations.

Regarding the diffraction patterns for bulk and nanoparticles of different sizes, Figures S18 and S19, we can observe these peak broadening effects and the change in the intensity of diffracted radiation with size, as expected, so that for NPs with up to 768 atoms, in the case of ceria, and 1500, in the case of tetragonal zirconia, these effects are more evident, given the difference in particle behavior relative to bulk, so that these behavior details can be explained in terms of the size limitation associated with the structure factor. From the respective sizes of such NP, the position and multiplicity of the peaks coincide for bulk and nanoparticle, and according to what is found in the literature[9,10], the difference in the diffraction patterns is reduced with increasing size.

However, the diffraction patterns of monoclinic zirconia (which includes the position of the peaks) do not coincide with each other and with those found in the literature, even for a

bulk representing 2592 atoms, which may have happened because the force field was originally parameterized for ceria, with a fluorite-like crystalline structure,[11] and therefore may not adequately describe the behavior of zirconia NP. Probably for this reason, bulk behavior in tetragonal zirconia starts to occur for a larger particle compared to ceria.

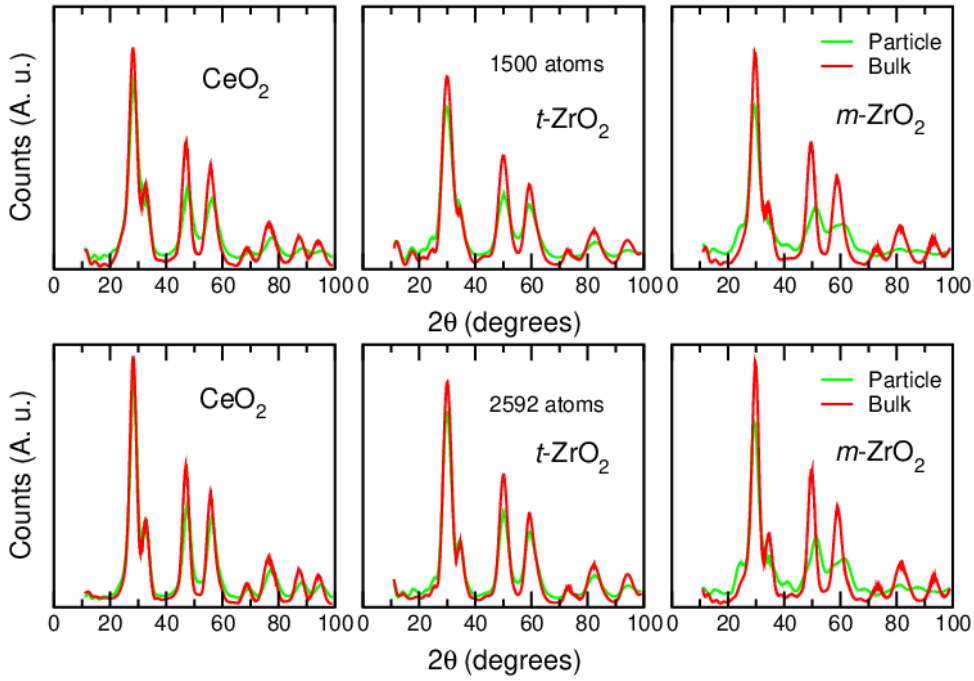

Figure S19: X-ray diffraction results for bulk and NPs of CeO_2, *t*-ZrO_2 and *m*-ZrO_2 with 500 and 864 cations.

S4.4 Energies from MD, MM and DFT Calculations

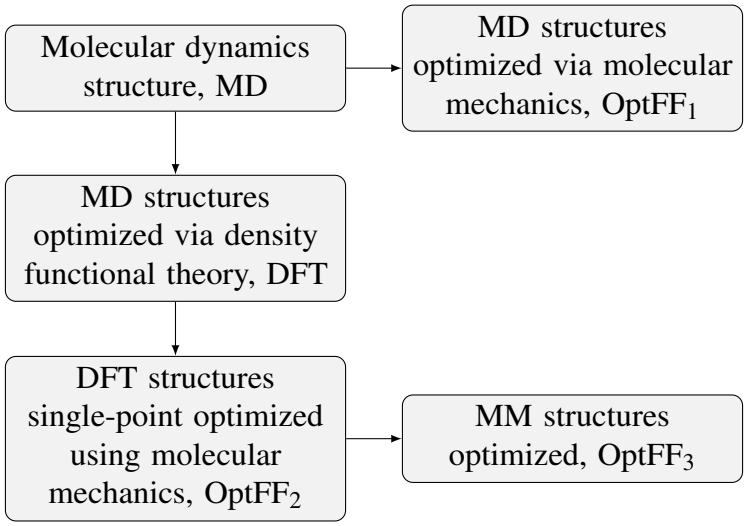

Figure S20: Flowchart detailing the acronyms in the Table S3.

Table S3: Different energies referring to the lowest energy structures in molecular dynamics, MD, MD structures optimized through molecular mechanics simulations, $OptFF_1$, MD structures optimized with DFT calculations, DFT, structures resulting from DFT after single point calculation of MM, $OptFF_2$, and these structures, finally optimized with the MM, $OptFF_3$. Energy values are in eV.

Size	x	System	MD	$OptFF_1$	DFT	$OptFF_2$	$OptFF_3$
32 cations	0.0	$Ce_{32}O_{64}$	−3293.70	−3293.70	−745.02	−3275.51	−3293.70
	0.2	$Ce_{26}Zr_6O_{64}$	−3328.47	−3328.47	−782.47	−3307.97	−3328.47
	0.4	$Ce_{19}Zr_{13}O_{64}$	−3370.80	−3370.80	−826.68	−3348.13	−3370.80
	0.6	$Ce_{13}Zr_{19}O_{64}$	−3404.69	−3404.69	−860.74	−3381.40	−3404.69
	0.8	$Ce_6Zr_{26}O_{64}$	−3445.28	−3445.28	−905.21	−3418.11	−3445.28
	1.0	$Zr_{32}O_{64}$	−3480.92	−3480.92	−941.38	−3455.68	−3480.92
40 cations	0.0	$Ce_{40}O_{80}$	−4121.08	−4121.08	−933.91	−4094.96	−4121.08
	0.2	$Ce_{32}Zr_8O_{80}$	−4169.57	−4169.57	−985.13	−4149.03	−4169.57
	0.4	$Ce_{24}Zr_{16}O_{80}$	−4217.76	−4217.76	−1033.24	−4190.47	−4217.76
	0.6	$Ce_{16}Zr_{24}O_{80}$	−4265.17	−4265.17	−1082.47	−4236.66	−4265.17
	0.8	$Ce_8Zr_{32}O_{80}$	−4312.97	−4312.97	−1133.12	−4280.16	−4312.97
	1.0	$Zr_{40}O_{80}$	−4357.72	−4357.72	−1180.50	−4323.99	−4357.72
56 cations	0.0	$Ce_{56}O_{112}$	−5789.58	−5789.58	−1322.67	−5760.31	−5789.47
	0.2	$Ce_{45}Zr_{11}O_{112}$	−5849.90	−5849.90	−1379.51	−5809.11	−5849.82
	0.4	$Ce_{34}Zr_{22}O_{112}$	−5914.55	−5914.55	−1448.65	−5873.81	−5914.55
	0.6	$Ce_{22}Zr_{34}O_{112}$	−5987.18	−5987.18	−1524.85	−5948.50	−5987.18
	0.8	$Ce_{11}Zr_{45}O_{112}$	−6050.46	−6050.46	−1593.24	−6002.64	−6050.46
	1.0	$Zr_{56}O_{112}$	−6113.53	−6113.53	−1660.59	−6062.40	−6113.48
72 cations	0.0	$Ce_{72}O_{144}$	−7461.67	−7461.67	–	–	–
	0.2	$Ce_{58}Zr_{14}O_{144}$	−7540.41	−7540.41	–	–	–
	0.4	$Ce_{43}Zr_{29}O_{144}$	−7619.58	−7619.58	–	–	–
	0.6	$Ce_{29}Zr_{43}O_{144}$	−7699.72	−7699.72	–	–	–
	0.8	$Ce_{14}Zr_{58}O_{144}$	−7787.03	−7787.03	–	–	–
	1.0	$Zr_{72}O_{144}$	7870.47	−7870.47	–	–	–
108 cations	0.0	$Ce_{108}O_{216}$	−11 221.15	−11 221.15	–	–	–
	0.2	$Ce_{86}Zr_{22}O_{216}$	−11 344.87	−11 344.87	–	–	–
	0.4	$Ce_{65}Zr_{43}O_{216}$	−11 461.43	−11 461.43	–	–	–
	0.6	$Ce_{43}Zr_{65}O_{216}$	−11 581.87	−11 581.87	–	–	–
	0.8	$Ce_{22}Zr_{86}O_{216}$	−11 699.23	−11 699.23	–	–	–
	1.0	$Zr_{108}O_{216}$	−11 826.25	−11 826.25	–	–	–
140 cations	0.0	$Ce_{140}O_{280}$	−14 567.46	−14 567.46	–	–	–
	0.2	$Ce_{112}Zr_{28}O_{280}$	−14 727.00	−14 727.00	–	–	–
	0.4	$Ce_{84}Zr_{56}O_{280}$	−14 880.88	−14 880.88	–	–	–
	0.6	$Ce_{56}Zr_{84}O_{280}$	−15 036.88	−15 036.88	–	–	–
	0.8	$Ce_{28}Zr_{112}O_{280}$	−15 186.50	−15 186.50	–	–	–
	1.0	$Zr_{140}O_{280}$	−15 348.16	−15 348.16	–	–	–
198 cations	0.0	$Ce_{198}O_{396}$	−20 642.48	−20 642.48	–	–	–
	0.2	$Ce_{158}Zr_{40}O_{396}$	−20 862.82	−20 862.82	–	–	–
	0.4	$Ce_{119}Zr_{79}O_{396}$	−21 075.07	−21 075.07	–	–	–

Continues on the next page

	0.6	$Ce_{79}Zr_{119}O_{396}$	−21 301.18	−21 301.18	–	–	–
	0.8	$Ce_{40}Zr_{158}O_{396}$	−21 523.64	−21 523.64	–	–	–
	1.0	$Zr_{198}O_{396}$	−21 739.50	−21 739.50	–	–	–
256 cations	0.0	$Ce_{256}O_{512}$	−26 725.86	−26 725.87	–	–	–
	0.2	$Ce_{205}Zr_{51}O_{512}$	−27 004.00	−27 004.00	–	–	–
	0.4	$Ce_{154}Zr_{102}O_{512}$	−27 285.16	−27 285.16	–	–	–
	0.6	$Ce_{102}Zr_{154}O_{512}$	−27 561.21	−27 561.21	–	–	–
	0.8	$Ce_{51}Zr_{205}O_{512}$	−27 859.40	−27 859.40	–	–	–
	1.0	$Zr_{256}O_{512}$	−28 139.54	−28 139.54	–	–	–

S4.5 Excess Energy with Parabolic Fitting

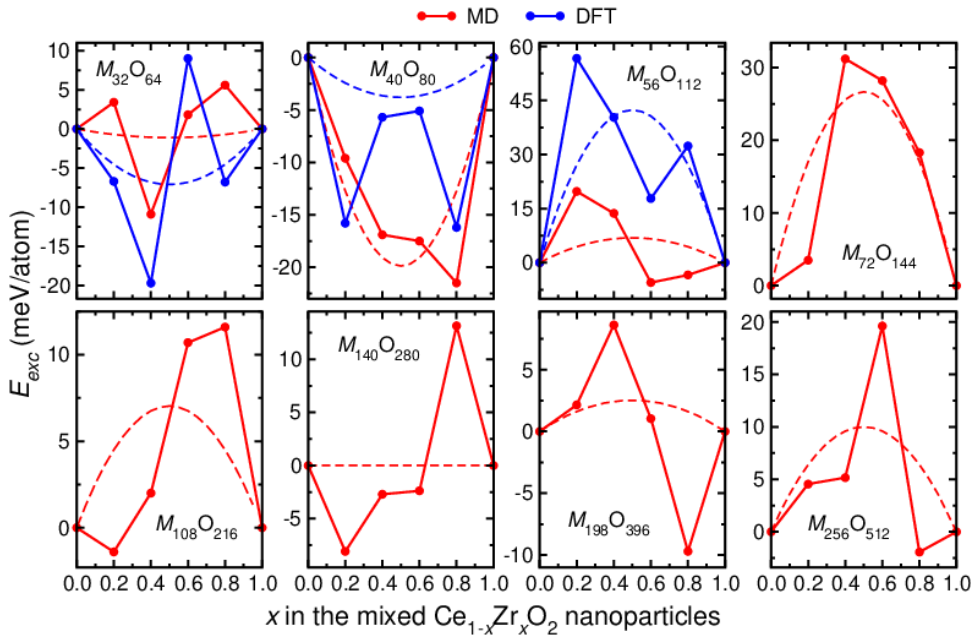

Figure S21: Results for the excess energy for all the $Ce_{1-x}Zr_xO_2$ NPs: Molecular dynamics and density functional theory results with parabolic fitting.

References

1 Verlet, L. Computer "experiments" on Classical Fluids. I. Thermodynamical Properties of Lennard-Jones Molecules. *Physical Review* **1967**, *159*, 98–103, DOI: 10.1103/physrev.159.98.

2 Allen, M. P. *Computer Simulation of Liquids*; Oxford University Press, 2017.

3 González, M. Force Fields and Molecular Dynamics Simulations. *École thématique de la Société Française de la Neutronique* **2011**, *12*, 169–200, DOI: 10.1051/sfn/201112009.

4 Ke, Q.; Gong, X.; Liao, S.; Duan, C.; Li, L. Effects of Thermostats/Barostats on Physical Properties of Liquids by Molecular Dynamics Simulations. *Journal of Molecular Liquids* **2022**, *365*, 120116, DOI: 10.1016/j.molliq.2022.120116.

5 Braun, E.; Gilmer, J.; Mayes, H. B.; Mobley, D. L.; Monroe, J. I.; Prasad, S.; Zuckerman, D. M. Best Practices for Foundations in Molecular Simulations [Article v1.0]. *LiveCoMS* **2018**, *1*, 5957.

6 de Mendonça, J. P. A.; Lourenço, T. C.; Freitas, L. P. M.; Santo, A. A. E.; Feliciano, G. T.; Da Silva, J. L. F. Molecular Dynamics Investigation of the Structural and Energetic Properties of $CeO_2 - MO_x$ (M = Gd, La, Ce, Zr) Nanoparticles. *Materials Advances* **2021**, *2*, 7759–7772, DOI: 10.1039/D1MA00543J.

7 Li, T.; Senesi, A. J.; Lee, B. Small Angle X-ray Scattering for Nanoparticle Research. *Chemical Reviews* **2016**, *116*, 11128–11180, DOI: 10.1021/acs.chemrev.5b00690.

8 Marshall, T. C. Kinetic Monte Carlo Simulation of Binary Alloys. **2018**,

9 Pouretedal, H. R.; Tofangsazi, Z.; Keshavarz, M. H. Photocatalytic Activity of Mixture of ZrO_2/SnO_2, ZrO_2/CeO_2 and SnO_2/CeO_2 Nanoparticles. *Journal of Alloys and Compounds* **2012**, *513*, 359–364, DOI: 10.1016/j.jallcom.2011.10.049.

10 Suresh, R.; Ponnuswamy, V.; Mariappan, R. Effect of Annealing Temperature on the Microstructural, Optical and Electrical Properties of CeO_2 Nanoparticles by Chemical Precipitation Method. *Applied Surface Science* **2013**, *273*, 457–464, DOI: 10.1016/j.apsusc.2013.02.062.

11 Minervini, L.; Grimes, R. W.; Sickafus, K. E. Disorder in Pyrochlore Oxides. *Journal of the American Ceramic Society* **2004**, *83*, 1873–1878, DOI: 10.1111/j.1151-2916.2000.tb01484.x.